Robustness of inverse solutions for radiative transfer parameters from light signals measured with different detection configurations

Yonghong Qin [a,b,c,d,1], Peng Tian [a,b,c,e,1,*], Lin Zhao [a,d], Stephen M. Mutisya [b], Jiahong Jin [a,b,c,e], Jun Q. Lu [b,a], Xin-Hua Hu [b,a,*]

[a] *Institute for Advanced Optics, Hunan Institute of Science and Technology, Yueyang, Hunan, 414006, China*
[b] *Department of Physics, East Carolina University, Greenville, NC, 27858, USA*
[c] *Key Laboratory of Hunan Province on Information Photonics and Optical Communication, Hunan Institute of Science and Technology, Yueyang, Hunan, 414006, China*
[d] *School of Information Science and Technology, Hunan Institute of Science and Technology, Yueyang, Hunan, 414006, China*
[e] *School of Physics & Electronic Science, Hunan Institute of Science and Technology, Yueyang, Hunan, 414006, China*

ABSTRACT

Spectroscopic characterization of turbid samples needs to solve inverse scattering problems (ISPs). With the radiative transfer (RT) theory as the framework for modeling light-matter interaction, accurate characterization becomes feasible but practical implementation remains challenging. We have evaluated the uniqueness and robustness of ISP solutions for a multiparameter spectrophotometer system without integrating spheres using different detection configurations for signal measurement. A novel parameter of area descending rate (ADR) has been developed to sample globally the distribution of an objective function in the 3D space of RT parameters and quantify uniqueness and robustness of ISP solutions. Analysis of the objective function for different sample types show the uniqueness of solutions for different detection configurations with increased complexity for samples of very larger single-scattering albedo values. The robustness of ISP solutions as quantified by ADR was found to be insensitive to the changes in detection configurations. Such stability provides strong evidences that the multiparameter spectrophotometry using only three photodiodes combined with Monte Carlo simulations yields a valuable and practical approach for turbidity characterization.

Published by Elsevier Ltd.

1. Introduction

Conventional spectrophotometry is perhaps the most frequently used means for material analysis, which acquires one signal of collimated transmittance T_c from a sample of thickness D as function of wavelength λ [1,2]. Either spectral data of absorbance or attenuation coefficient can be determined respectively as $A(\lambda) = \log(1/T_c(\lambda))$ or $\mu_t(\lambda) = 2.30A(\lambda)/D$ based on the Beer-Lambert law. Nevertheless, it lacks the ability to determine absorption and scattering parameters of turbid samples including biological tissues and cell suspensions. Various approaches of turbidity characterization have been investigated beyond the simple Beer-Lambert law. In all cases, multiple signals of scattered light are to be acquired and inverse scattering problems (ISPs) are to be solved for retrieval of optical parameters, which requires quantitative modeling of absorption and scattering processes. Light transport in a turbid sample of size much larger than wavelengths of interrogating light can be accurately modeled by the radiative transfer (RT) theory [3]. Within this framework, the absorption coefficient $\mu_a(\lambda)$, scattering coefficient $\mu_s(\lambda)$ and anisotropy factor $g(\lambda)$ are inversely determined from measured signals to yield an improved form of spectrophotometry. Determination of above parameters at different wavelengths by solving ISPs defined by the RT theory is termed as the multiparameter spectrophotometry in this report. The following steady-state and source-free equation defines the RT parameters [3]

$$\mathbf{s} \cdot \nabla L(\mathbf{r}, \mathbf{s}) = -(\mu_a + \mu_s)L(\mathbf{r}, \mathbf{s}) + \mu_s \int_{4\pi} p(\mathbf{s}, \mathbf{s})' L(\mathbf{r}, \mathbf{s})' d\omega', \quad (1)$$

where $L(\mathbf{r}, \mathbf{s})$ is the light radiance at location $\mathbf{r}$ along direction of unit vector $\mathbf{s}$, $p(\mathbf{s}, \mathbf{s}')$ is the single-scattering phase function describing local distribution of light scattered from $\mathbf{s}'$ to $\mathbf{s}$ and $d\omega'$ is elementary solid angle along $\mathbf{s}'$. If light scattering is assumed axial symmetric, then one has $p(\mathbf{s}, \mathbf{s}') = p(\cos\theta)$ with $\cos\theta = \mathbf{s} \bullet \mathbf{s}'$ and θ as the scattering polar angle. The ensemble averaged value

---

of $\cos\theta$ or $<\cos\theta>$ yields the anisotropy factor g with p used as a distribution function.

Extensive studies have been reported over the past few decades on multiparameter spectrophotometry [4–14]. The most popular approach of implementation is to acquire three light signals with one or two integrating spheres for retrieval of the RT parameters. The use of integrating spheres allows measurement of hemispherical diffuse reflectance R_h and diffuse transmittance T_h. Collimated transmittance T_c or forward transmittance T_f is also acquired. With T_c one can first determine μ_t ($= \mu_a + \mu_s$) and then solve ISPs from R_h and T_h in 2D parameter space of single-scattering albedo $a = \mu_s/\mu_t$ and g. Furthermore, the hemispherical acquisition enables algorithms for fast signal calculation, which include adding-doubling by assuming a sample of shape as an infinite plane-parallel slab or Monte Carlo (MC) simulations with high sampling efficiency for calculation of R_h and T_h [5,8]. If T_f instead of T_c is measured, accurate MC simulations with low sampling efficiency for calculation of T_f have to be performed to solve discrete ISPs in 3D space of RT parameters with high computational cost [9].

Despite the advantage of fast algorithms for signal calculation, the employment of integrating spheres leads to several limitations for translation into easy-to-use instruments like the conventional spectrophotometers. First, measurement of T_c for strongly turbid samples with g close to 1 requires removal of strong forward scatter by spatial filtering. This in turn increases the size and/or complexity of the optical setup and restricts the optical thickness $\tau = \mu_t D$ of the measured samples. For example, the value of T_c decreases to 3.4×10^{-4} or less once τ exceeds 10 for a turbid sample. At this signal level, it is very difficult to keep T_c from contamination by forward scatter and/or other noises [8]. Consequently, very thin samples must be prepared to make D around tens of micrometers with increased difficulty for sample assembly. Second, one needs to measure signals in at least two steps at each wavelength with one sphere. Two integrating spheres permit simultaneous measurement of R_h, T_h and possibly T_c (or T_f) in one step but needs extra care for system maintenance and sample assembly. Either way, longer time of data acquisition or substantial burden of sample assembly can plague wide applications of the integrating sphere based approach. Finally, integrating spheres merely redistribute scattered light over hemispherical surface and the same weak signals detection methods such as lock-in amplification is essential for signal measurement. With the added expenses for purchase and maintenance of integrating spheres, the total cost of ownership for instruments based on this approach can be considerably higher than those of conventional spectrophotometry.

Angle-resolved acquisition of scattered light signals has been investigated with various goniometric designs of signal detection. Such a system typically employs either multiple, about 20 or more, detectors in fixed positions or a scanning detector to acquire signals over multiple angles and then retrieve RT parameters from the measured signals [14]. This approach, however, is time-consuming for detector scanning or of low dynamic reserve for a multi-sensor design in comparison to phase sensitive detection of weak signals from limited number of detectors. These disadvantages make the goniometry approach unsuitable for developing general-purpose instruments for multiparameter spectrophotometry.

We have developed an alternative approach without integrating spheres to eliminate aforementioned deficiencies by taking the advantage of the steep decrease in computational cost over the past decade. A 3-photodiode design has been developed and investigated for rapid acquisition of signals and ISP solutions [15,16]. We have found that the sensitivity of acquired signals on the angular distribution of scattered light for an unknown sample can be reduced by sufficiently large solid angles for light collection by photodiodes. With the choice of an angularly smooth function such as

$p_{HG}(\cos\theta)$ for $p(\cos\theta)$, proposed by Heyney and Greenstein (HG) [17], efficient inverse algorithms can be crafted to retrieve the RT parameters [18]. The initial implementation still included T_c for determination of μ_t first followed by non-hemispherical measurement of the diffuse reflectance R_d and transmittance T_d. Modeling of light scattering and signal detection with MC simulations have been performed by a perturbation algorithm to rapidly determine a and g [15,19]. The above configuration of signal detection has been validated by comparing the inversely determined RT parameters of sphere suspensions against those obtained by the Mie theory [15]. Subsequent improvement has been made by replacing T_c with forward transmittance T_f in the measured signals from optically thick samples with τ up to 20 and markedly simplifies procedures for preparing strongly turbid samples [16,18]. Our results show that the key to prevent an ISP from unsolvable or ill-posted is to accurately model light transport through the sample assembly and collection by the 3-photodiode scheme for calculation of signals with high fidelity to the experimental system. It also has been demonstrated that the use of HG function is advantageous in comparison to Mie based phase function for MC calculated signals by improving the robustness of ISP solutions for sphere suspension samples of high concentrations [18].

The non-hemispherical detection presents an intriguing question on how variation in the configuration of the 3-photodiode detection scheme affects the robustness of ISP solutions for different sample types. In this report, we present the results of an in-depth study on solution robustness against detection configuration variation for different sample types by analyzing the contour lines of an objective function δ in the RT parameter space. A parameter of area descending rate (ADR) has been defined and tested to verify the existence and quantify robustness among multiple planes of (μ_s, g) at different μ_a values for a given ISP. Our results show that the maximum value of ADR points to the correct μ_a and a region in the corresponding (μ_s, g) plane for solving the ISP with reliability much improved in comparison to an iterative algorithm of gradient descent by δ alone, which can become unstable due to inherent fluctuations in δ by the variance of MC calculated signals. It has been demonstrated that the ISPs formed by the measured signals of R_d, T_d and T_f are of convex type with strong robustness for ISP solutions with different detector distances and angles of the 3-photodiode design.

2. Experimental and theoretical methods

2.1. Experimental system and sample preparation

An experimental system has been constructed to perform multiparameter spectrophotometry. The detection design is shown in Fig. 1 with 3 photodiodes of 3.6mm × 3.6mm in sensor area (FDS100, Thorlabs) to acquire the scattered light of intensity I_{Rd}, I_{Td} and I_{Tf} by D_2, D_3 and D_4 respectively. Another photodiode D_1 was used to monitor I_0 as the intensity of light incident on the sample assembly. The detection design can be modified by adjusting the distances and angles of the 3 photodiodes. For ease of analysis we define each detection configuration by a vector $\Psi = (d_R, d_T, d_f, \theta_R, \theta_T)$ with its elements defined in Fig. 1(A). The configuration vector Ψ was varied to investigate the robustness of ISP solutions to different designs. In addition, each detector was installed at the end of a black plastic tube for limiting its field of view to the front or back sample surface. The tubes are very effective to reduce background noise by light scattered from sample holder and other surrounding objects.

With a tunable monochromator, the wavelength λ can be varied from 460 to 1000 nm by a stepsize of 20 nm with a half-maximum bandwidth around 4.7 nm for adequate light intensity. The output beam was modulated by a mechanical chopper at a fre-
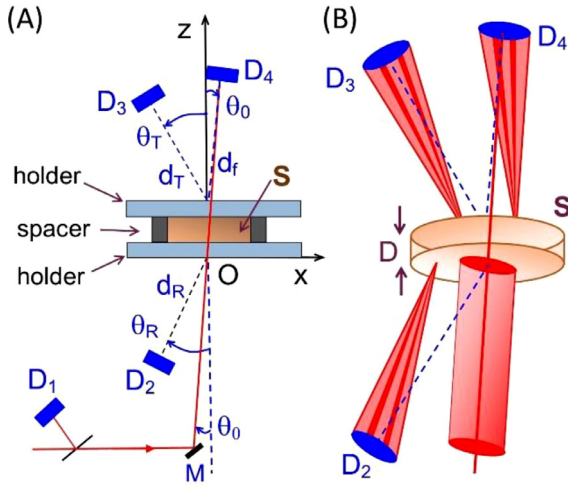
Fig. 1. (A) Schematic of sample and detection configuration: M = mirror, S = sample, θ_0 = incident angle, θ_R and d_R (θ_T and d_T) = angle and distance of D_2 (D_3) for measuring R_d (T_d), d_f = distance of D_4 for measuring T_f; (B) perspective view of light collection cones for 3 detectors with each having a field of view over the front or back surface of sample: D = sample thickness. For clarity, the holder glass slabs, spacer and black tubes to limit field of view of detectors are not shown.

quency of f_0 = 385 Hz before the monochromator. Output signals from the detectors were pre-amplified and fed into an in-house built 4-channel lock-in board connected to a computer to acquire the signals at f_0. At each wavelength, 3 measured signals were determined as $R_d = I_{Rd}/I_0$, $T_d = I_{Td}/I_0$ and $T_f = I_{Tf}/I_0$.

Suspension samples of polystyrene spheres were prepared for validating our method against the RT parameters calculated by the Mie theory under the assumption of single and independent sphere in light scattering. The suspension was confined within a ring-shaped spacer between two glass slides of about 1mm in thickness for each. The spacer defines the suspension sample shape with thickness D = 2.10±0.1 mm and inner diameter of 14.3 mm. Multiple samples were made by diluting commercial sphere suspensions of different nominal diameters d_s with deionized water [16]. For this study, we selected the measured signals from one sample of d_s = 11 μm with coefficient of variance (CV) ≤ 18% (7510B, ThermoFisher Scientific). We chose this sample because these spheres have sizes close to those of human epithelial cells and μ_a values of sphere suspension estimated by the Mie theory are above the lower limit of measurement by our method for strongly turbid samples [16]. The number density ρ_s of spheres in the suspension sample was determined by the masses of suspension and dry sphere component and found to be (3.05±0.02)x10^4 mm^{-3} using an evaporation method [20]. The mean value and standard deviation of sphere diameters were determined respectively to be 11.5 μm and 1.0 μm with a microscope and its distribution was found to be Gaussian [18].

2.2. Monte Carlo simulations

An individual photon tracking MC (iMC) code has been built to calculate signals with the detection configuration illustrated in Fig. 1(A). Details of the code algorithm, validation results and implementation on a graphic processing unit (GPU) board have been previously published and are briefly described below [6,8,19,21,22]. An incident light beam is represented in iMC by N_0 photons injected on the front surface of sample holder in an ellipse defined by the measured beam profile with an incident angle of θ_0 indicated in Fig. 1(A). The RT parameters for optical characterization of a sample are expressed by a vector $\mathbf{P} = (\mu_a, \mu_s, g)$ for each wavelength together with a set of size parameters for the sample,

spacer and holder glasses. A total length L_a is determined from μ_a and a random number (RN) uniformly distributed in (0,1) for each photon before tracking starts. Then each photon propagates through or becomes reflected off various index mismatched interfaces among air, holder glass slab, spacer and sample according to the local Fresnel reflectance. Once a photon moves into the turbid sample, its trajectory evolves as a sequence of line segments with pathlengths L_{sj} (j = 1, 2, …) determined by μ_s and RNs. The polar angle θ and azimuthal angle φ of scattering are updated by a chosen single-scattering phase function. Based on our previous study for sphere suspensions of high concentration [18], the HG function was applied to derive θ with RN and φ with RN only. At the end of L_{sj}, the accumulated pathlength $L_s = \sum_{j\prime=1}^{j} L_{sj}\prime$ is compared to L_a. If $L_s \geq L_a$, the photon is terminated as an absorption event; otherwise it is propagated further until a sample surface is reached. When the photon exits the sample assembly into air, the code further determines its exit location and directional cosines. The photon counter for a detector is incremented if the photon hits it within its angular cone of collection as illustrated in Fig. 1(B). Finally, the calculated signals of R_{dc}, T_{dc} and T_{fc} are obtained as the ratios of the number of photons collected by a respective detector to N_0 once tracking ends.

2.3. Analysis of objective function in RT parameter space

An objective function δ is defined as the sum of squared errors between the measured (or equivalent) and calculated signals as follows

$$\delta(\mathbf{P}, \mathbf{\Psi}) = \left(\frac{R_d - R_{dc}}{R_d}\right)^2 + \left(\frac{T_d - T_{dc}}{T_d}\right)^2 + \left(\frac{T_f - T_{fc}}{T_f}\right)^2. \tag{2}$$

where R_{dc}, T_{dc} and T_{fc} are the calculated signals by the iMC code. Different samples and detection configurations were used in this study to evaluate the robustness of ISP solutions by the multiparameter spectrophotometry method presented here. For the sphere sample, we denote the detection configuration of experimental system as $\mathbf{\Psi}_0$ and the modified configurations as $\mathbf{\Psi}_m$. For virtual samples with smaller values of scattering albedo a or g, the RT parameter vector is defined by $\mathbf{P}_v = (\mu_{av}, \mu_{sv}, g_v)$. Because no measured signals are available for $\mathbf{\Psi}_m$ or $\mathbf{P}_v$, the values of the measured signals of R_d, T_d and T_f in Eq. (2) were replaced by the "equivalent" signals calculated by the iMC code with $\mathbf{\Psi}_m$ or $\mathbf{P}_v$.

All ISPs analyzed in this study have been solved as optimization problems given by

$$\begin{aligned} \text{minimize} \quad & \delta(P, \mathbf{\Psi}), \\ \text{subject to} \quad & P: \mu_a, \mu_s > 0, \ -1 \leq g \leq 1; \\ & \mathbf{\Psi}: d_R, d_T, \ d_f > 0; \ 0° < \theta_R, \theta_T < 90°. \end{aligned} \tag{3}$$

An ISP solution is deemed as unique when δ reaches a minimum value δ_{min} and satisfies the condition of $\delta_{min} < \delta_0$ for a unique vector $\mathbf{P}$. The threshold value δ_0 was set to 0.75% since the relative errors of the measured signals were estimated to be around ±5% by three repeated measurements at each wavelength [16,18]. To investigate the robustness of a discrete ISP solution, we performed large numbers of iMC simulations to examine distribution of the δ function in the 3D space of RT parameters.

Quantitative analysis of $\delta(\mathbf{P}, \mathbf{\Psi})$ distributions in the 3D parameter space is necessary to evaluate and compare different detection configurations. It has been found that computational cost can be significantly reduced by quantifying δ distributions in 2D planes of (μ_s, g) at selected values of μ_a. Contour lines of $\delta(\mathbf{P}, \mathbf{\Psi})$ were obtained by iMC simulations followed by interpolation in the 2D planes for ISP evaluation. The contour line analysis significantly reduced the effect of variance inherent in the iMC simulations and different parameters were extracted and compared. An averaged

Table 1

The measured signals and RT parameters by the Mie theory at two wavelengths [a]

λ (nm)	Measured signals [a]			$\mathbf{P}_M(\lambda)$ [b]		
	$R_d \times 10^4$	$T_d \times 10^4$	$T_f \times 10^4$	μ_{aM} (mm^{-1})	μ_{sM} (mm^{-1})	g_M
500	4.54±0.13	4.16±0.13	1.56±0.076	0.253	6.16	0.927
800	4.56±0.034	4.02±0.063	1.37±0.0054	0.251	5.56	0.915

[a] The signals were acquired with $\mathbf{\Psi}_0$ of d_R = 21.5 mm, θ_R = 45°, d_T = 35.7 mm, θ_T = 48°, d_f = 88.4 mm.

[b] Mean and standard deviation were obtained by 3 measurements of signals and $\mathbf{P}_M(\lambda)$ components were calculated with the measured sphere concentration $\rho_s = 3.05 \times 10^4$ mm^{-3}.

slope of contour area change in (μ_s, g) plane was selected as an effective metric to quantify the convergence speed toward an ISP solution. This approach was then applied to characterize the ISP type and robustness among various detection configurations of $\mathbf{\Psi}_0$ and $\mathbf{\Psi}_m$ for different sample types.

To speed up further, the iMC code has been implemented for parallel execution on a GPU board (GeForce RTX 2080 Ti, Nvidia). Simulation time depends mainly on total photon number N_0, μ_a, μ_s and sample size. For a sample of μ_a = 0.290 mm^{-1}, μ_s = 6.56 mm^{-1} and D = 2.10 mm in this study, it took about 2 s to complete tracking of photons with $N_0 = 1 \times 10^8$. The averaged variance in calculated signals of R_{dc}, T_{dc} and T_{fc} in the above example is about 0.6% due to the statistical nature of MC simulations.

3. Results and discussion

3.1. Code validation against Mie results

Measurements of R_d, T_d and T_f were repeated three times at each wavelength λ with the 3 photodiodes in the configuration of $\mathbf{\Psi}_0$. To validate the experimental system and iMC code, a Matlab code of the Mie theory was employed to obtain the total absorption cross section σ_a, total scattering cross section σ_s and anisotropy factor g_M of a single sphere. The values of λ, d_s and refractive indices of n_s for the sphere and n_h for the host medium of water were used as the input parameters to the Mie code [20,23]. Afterwards, the RT parameters were determined as $\mathbf{P}_M = (\mu_{aM}, \mu_{sM}, g_M) = (\rho_s\sigma_a, \rho_s\sigma_s, g_M)$, which are based on the assumption of spheres in a suspension sample being independent, of same diameter and, uniform distribution. Table 1 presents the measured signals and $\mathbf{P}_M(\lambda)$ and the averaged values of errors in measured signals were found to be around ±3%.

We have performed iMC simulations for calculated signals and determined $\delta(\mathbf{P}, \mathbf{\Psi}_0)$ with measured signals of the sphere sample at λ = 500 and 800 nm. The input parameters for iMC included incident beam profile, sizes and positions of sample, holder and detectors by $\mathbf{\Psi}_0$. A restricted search was initially performed in the region near $\mathbf{P}_M(\lambda)$ as listed in Table 1 with μ_a and g kept close to μ_{aM} and g_M and the obtained RT parameters are denoted as $\mathbf{P}_1(\lambda)$. At either of the two λ values, a unique solution of μ_s can be obtained with minimal δ satisfying $\delta_{min} < \delta_0$. Fig. 2 shows the calculated signals and δ values against μ_s for λ = 500 nm. While R_{dc} rises approximately linearly with μ_s, the diffuse transmittance T_{dc} rises initially with increasing μ_s for stronger multiple scattering and then decreases because of boosted reflectance. The exponential drop of T_{fc} for increasing $\mu_s < 3$ mm^{-1}, on the other hand, shows clearly its dominance by the collimated transmitted light which follows the Beer-Lambert law. When μ_s exceeds 4 (mm^{-1}) or optical thickness $\mu_t D \approx \mu_s D > 8$, T_{fc} is dominated by forward scatter with a very gentle decline for increasing μ_s. It is obvious from the $\delta(\mu_s)$ curve in Fig. 2 that the optimization problems associated with ISP is of convex type for fixed μ_a and g.

By restricted search, an inverse solution was obtained as $\mathbf{P}_1$(500 nm) = (0.228 mm^{-1}, 6.31 mm^{-1}, 0.920) with δ_{min} and μ_{s1} indicated in Fig. 2. Similar result was obtained for the sphere sample
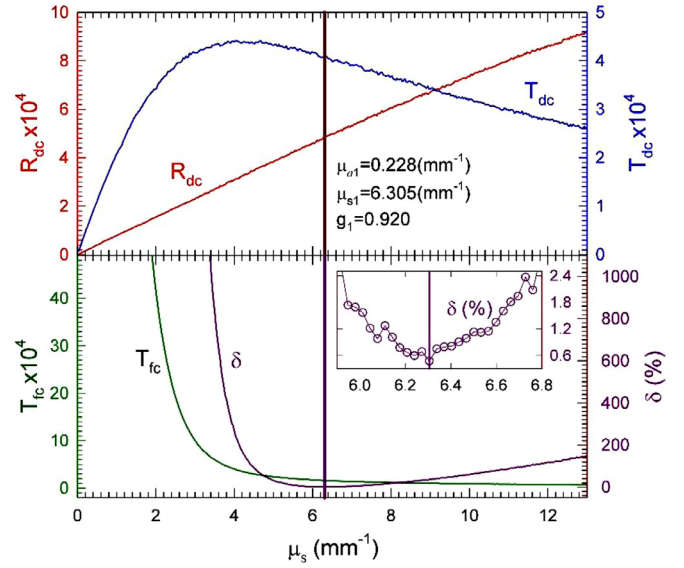

Fig. 2. The calculated signals and objective function δ versus μ_s obtained with the measured signals from the sphere sample of d_s = 11μm at λ = 500 nm and fixed values of μ_{a1} = 0.228 mm^{-1} and g_1 = 0.920. Inset: plot of $\delta(\mu_s)$ on expanded scales with symbols representing calculated values and line as visual guide. The vertical lines indicate μ_{s1} of $\mathbf{P}_1$ with δ_{min} = 0.474% and tracked photon number $N_0 = 10^8$ for each iMC simulation.

at λ = 800 nm as $\mathbf{P}_1$(800 nm) = (0.248 mm^{-1}, 6.28 mm^{-1}, 0.916) with δ_{min} = 0.619%. Under the condition of keeping g close to g_M by the Mie theory, these results demonstrate that the ISP solutions of $\mathbf{P}_1(\lambda)$ obtained from the measured signals agree fairly well with $\mathbf{P}_M(\lambda)$ in Table 1 by the Mie theory with the assumption of treating spheres in suspension as independent particles for their interaction with light. We also note that the visible fluctuations in δ near δ_{min} as shown in the inset of Fig. 2 are due to the statistical variances in the calculated signals by iMC simulations. To reduce such an effect, one needs to find methods for global sampling of δ distributions in the RT parameter space.

3.2. Analysis of robustness by contour lines

It should be pointed out that solving ISPs by search on μ_s only may not provide a global solution of Eq. (3) in the 3D parameter space. We obtained and analyzed the contour lines of $\delta(\mathbf{P}, \mathbf{\Psi}_0)$ on multiple 2D planes of (μ_s, g) with different μ_a values. Fig. 3 presents examples of the contour plots for $\delta(\mathbf{P}, \mathbf{\Psi}_0)$ in two planes of (μ_s, g) for each λ value. Comparison of the plots at the same wavelength shows unambiguously that the optimization problem defined in Eq. (3) is of convex type with δ approaching to a unique minimum value δ_{min}. Close examination of contour plots further indicates that the planes containing smallest δ values close to or less than δ_0 also exhibit large rates of area decrease among the contour lines of decreasing δ values. A plane at μ_a = 0.248 mm^{-1} is presented in Fig. 3(B) as an example that exhibits much more grid points of $\delta < 1$% with δ_{min} = 0.398% than the one at
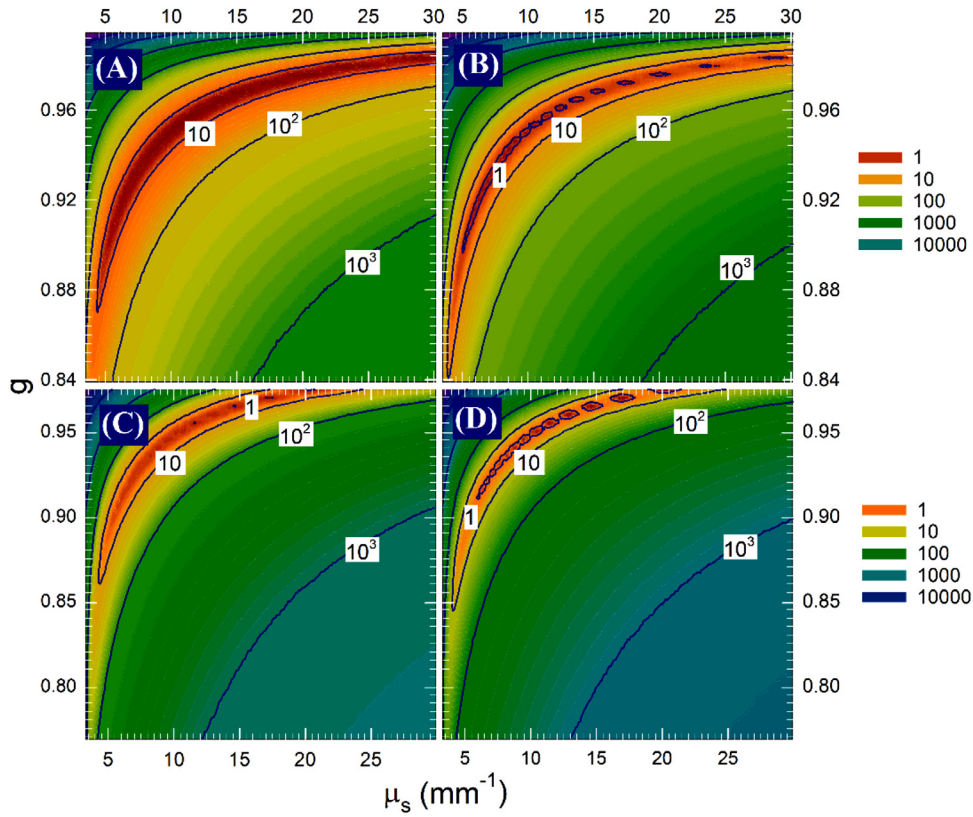
Fig. 3. Contour plots of $\delta(\mathbf{P}, \mathbf{\Psi}_0)$ in (μ_s, g) planes for the sphere sample at different values of μ_a and λ: (A) 0.208 mm^{-1}, 500 nm; (B) 0.248 mm^{-1}, 500 nm; (C) 0.228 mm^{-1}, 800 nm; (D) 0.248 mm^{-1}, 800 nm. The δ values in percentage are marked on selected contour lines and the legends of (B) and (D). The tracked photon number $N_0 = 10^8$ and total number of iMC simulations were 10449 for each plot.

$\mu_a = 0.208$ mm^{-1} in Fig. 3(A) with $\delta_{min} = 2.02\%$ for the case of $\lambda = 500$ nm. Similar results were obtained for $\lambda = 800$ nm, in which the plane in Fig. 3(D) with $\delta_{min} = 0.133\%$ should be selected for solving the ISP in comparison to the one in Fig. 3(C) with $\delta_{min} = 0.823\%$.

Examination of these data also demonstrates the increasing effect of variance for calculated signals by iMC simulations when δ approaching δ_0 around 1%, which can be observed in the inset of Fig. 2 as well. To significantly reduce the effect of variance without increasing the number of tracked photons in iMC simulations, the distribution of $\delta(\mathbf{P}, \mathbf{\Psi}_0)$ should be globally sampled to yield valid markers that can indicate the correct search direction for an ISP solution in the 3D space of RT parameters. After contour plot analysis at different (μ_s, g) planes similar to those in Fig. 3, we have gained insights on correct identification of μ_a and associated (μ_s, g) plane for solving Eq. (3). Several metrics based on the area change of contour lines have been conceived and tested. An area descending rate (ADR) parameter of $R_A(\mathbf{P}, \mathbf{\Psi})$ was eventually chosen as the parameter to quantify convergence speeds of inverse solutions in a plane of (μ_s, g).

To obtain ADR, C contour lines were selected with ascending δ values given by (δ_1, ..., δ_C) and the enclosed areas were calculated as $A(\delta_i)$ with i = 1, ..., C. The numbers of iMC simulations can be reduced by adding linearly interpolated points to the grid of μ_s and g used for simulations to accurately determine the contour lines. A weighting factor of $\delta_1/\delta_i A_{m,i}$ was used to emphasize those terms with smaller δ values and areas in ADR with $A_{m,i}$ as the mean value of $A(\delta_{i+1})$ and $A(\delta_i)$. With these considerations, the ADR parameter is defined by

$$R_A(\mathbf{P}, \mathbf{\Psi}) = \frac{1}{C}\sum_{i=1}^{C-1} H[A(\delta_i) - A_{th}]\frac{\delta_1}{\delta_i}\frac{A(\delta_{i+1}) - A(\delta_i)}{A_{m,i}(\delta_{i+1} - \delta_i)}. \qquad (4)$$

where H[...] is the Heaviside function to exclude a term from the sum in the case of $A(\delta_i)$ less than a threshold A_{th}. For all results presented here, A_{th} took out only the term of i = 1 in the sum for very few cases as noted below. Positive ADR values indicate area reduction as δ decreases toward δ_1 and their magnitudes measure the convergence speed for solving Eq. (3) among the selected (μ_s, g) planes. The use of multiple contour lines and the weighted sum of area descending rates reduce significantly the sensitivity of ADR to δ fluctuation that is important for correct choice of search direction by gradient descent. Thus, ADR value was used in this study to evaluate concerned ISP solutions and quantify the effect of detection configurations on solution robustness. We chose a set of 5 contour lines given by (1%, 2.5%, 4%, 7%, 10%) and 4-fold increase in grid points of (μ_s, g) by interpolation for contour calculation.

3.3. Accurate ISP solutions by ADR for sphere sample

By global sampling, ADR suppresses effectively fluctuations in δ distribution in searching for an ISP solution. A maximum ADR value for the (μ_s, g) plane at μ_a determines the correct value of μ_a for the fastest convergence rate in δ and a small region in the plane for solving ISP subsequently. The computational cost for ADR can be kept reasonable by fast iMC simulations and interpolation over 2D grids. Fig. 4 compares ADR values of 9 different planes of (μ_s, g) with the measured signals from the sphere sample for $\lambda = 500$ and 800 nm. Only 765 iMC simulations were carried out for each bar and the results clearly demonstrate the ability of maximum ADR values for accurately finding μ_a as corroborated by the contour plots in Fig. 3 obtained with much larger number of iMC simulations.

With the maximum ADR values to determine μ_a and contour plots in Fig. 3(B) and 3(D) to determine μ_s and g, the Eq. (3) was
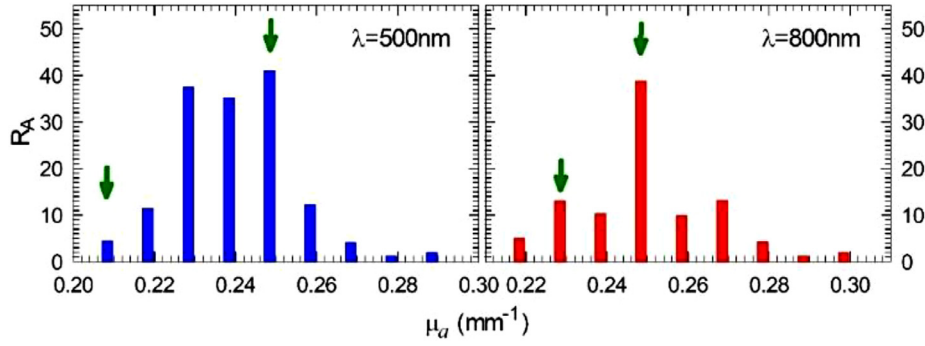
Fig. 4. ADR or $R_A(\mathbf{P}, \mathbf{\Psi})$ vs μ_a as the label for a plane of (μ_s, g) obtained with measured signals from the sphere sample at two λ values by $\mathbf{\Psi}_0$. The green arrows indicate the μ_a values of the contour plots in Fig. 3. The tracked photon number $N_0 = 10^8$ and total number of iMC simulations for each bar was set to 765.

solved in the 3D space of RT parameters. The results are expressed as $\mathbf{P}_2(\lambda)$ for the sphere sample at $\lambda = 500$ and 800 nm, which were given by $\mathbf{P}_2(500 \text{ nm}) = (0.248 \text{ mm}^{-1}, 8.45 \text{ mm}^{-1}, 0.943)$ with $\delta_{\min} = 0.398\%$ and $\mathbf{P}_2(800 \text{ nm}) = (0.248 \text{ mm}^{-1}, 14.5 \text{ mm}^{-1}, 0.965)$ with $\delta_{\min} = 0.133\%$. These values differ significantly from $\mathbf{P}_1(\lambda)$ obtained by restriction of $g(\lambda)$ values to be close to $g_M(\lambda)$ by the Mie theory as shown in Fig. 2, which does not correspond to the true minimal value of δ in the RT parameter space. The differences between $\mathbf{P}_2(\lambda)$ and $\mathbf{P}_M(\lambda)$ in Table 1 may be attributed to failure of independent particle assumption for interaction of light with the large spheres. We note first that the suspension samples of polystyrene spheres with diameters around or larger than 5 μm have observable settlement over periods of a few minutes despite their very close mass density to that of water. Even with manual shaking between wavelength changes during measurement, the sphere density can still deviate significantly from a constant for the suspension. Furthermore, aggregated spheres and interference of light scattered by nearby spheres in the layer of settled spheres can become substantial, leading to failure of independent sphere assumption for application of the Mie theory. In addition, the 3-photodiode design with only one detector collecting the forward light scatter may not provide sufficient information to accurately determine the RT parameters of the sphere samples that are of very high g values. This is corroborated by the large contour line areas in Fig. 3(B) and 3(D) for $\delta < \delta_0$ satisfied for a relatively large range of μ_s. In fact, these areas can be characterized by a long curved line of $\mu_s(g: \delta < \delta_0)$ which yields multiple permissible solutions in spite of the existence of unique $\delta_{\min}$. One possible solution is to add one or two detectors particularly near the T_f detector to provide an additional signal to increase the sensitivity of δ to μ_s by shrinking the line of $\mu_s(g: \delta < \delta_0)$. Additional studies are needed to clearly understand the light-sphere interactions for samples of high concentrations and fast settlement.

The use of maximum ADR values to determine μ_a provides also a novel approach for solving discrete ISPs defined in Eq. (3) with two-fold benefit in comparison to gradient descend based iterative algorithms. First, solving ISPs in the 3D space of RT parameters is simplified by a two-step process of 1D search for μ_a followed by solving ISPs in the 2D plane of (μ_s, g) at μ_a. Second, ADR allows faster iMC simulations by tracking less number of photons since summing δ values on multiple grid points for ADR calculation can effectively suppress δ fluctuation due to simulation variance. For example, close to 1000 iMC simulations can be completed by GPU execution within a minute if N_0 can be reduced from 5×10^7 to 1×10^7 to accurately determine ADR on a grid of (μ_s, g). This makes it possible to solve ISPs in real time, which could only be achieved previously by determination of μ_t from T_c. Development of a novel inverse algorithm by ADR is currently underway to investigate the lower limits of N_0 and number of iMC simulations needed for accurate interpolation and ADR calculations.

3.4. Effect of detection configuration on robustness for different sample types

In addition to solving an ITP, the parameter ADR provides a useful metric to compare robustness of solutions with different detection configurations. We formed different detection configurations represented by $\mathbf{\Psi}_m$ that were obtained by modifying one element of $\mathbf{\Psi}_0$ with others unchanged. For each $\mathbf{\Psi}_m$, the values of "equivalent" signals R_d, T_d and T_f in Eq. (2) were calculated by the iMC code using $\mathbf{P}_2(\lambda)$ as the RT parameters and $\mathbf{\Psi}_m$ as the modified configuration. Simulations of calculated signals were performed in the multiple (μ_s, g) planes of different μ_a values to determine δ and ADR for each $\mathbf{\Psi}_m$ and $\mathbf{\Psi}_0$ for the sphere sample at two wavelengths. Fig. 5 shows only the maximum ADR values for each configuration set of $\mathbf{\Psi}_m$ against $\mathbf{\Psi}_0$.

The sphere sample used in this study features strong turbidity and forward scattering due to its high values of a and g. As a result, the measured T_f signal is much larger than R_d and T_d if the 3 photodiodes were placed at similar distances from the sample. By adjusting detector distances from the sample we found experimentally that the stability of ISP solutions improves if the measured signals are kept on the same order of magnitude. The distance adjustment, however, must be implemented under two conditions. One is to have sufficient high signal-to-noise ratios for the measured signals and the other is to have adequate angular integration for collected light, which is necessary to reduce signals' sensitivity to detailed and unknown angular dependence of light scattering in the sample. The results in Fig. 5 verify these empirical guidelines used for non-hemispherical measurement of light scattering signals [15,16]. The distance $d_f = 88.4$mm of the T_f detector chosen for our experimental system shows the most robust performance for solving ISP at either λ. Changing from this value of d_f leads to deterioration in robustness of ISP solutions which is more severe in the case of $\lambda = 800$ nm. We also point out that the definition of δ function in Eq. (2) can be modified with weighting factors added among the three signal terms to improve the stability of ISP solutions if a detector configuration cannot be varied as described above.

To extend our study of detection optimization to other turbid sample types, we analyzed ADRs with virtual samples of smaller a and g values given by $\mathbf{P}_v = (\mu_{av}, \mu_{sv}, g_v)$ for different detection configurations. The values of scattering coefficient μ_s were decreased from those of the sphere sample to reduce simulation times. The function $\delta(\mathbf{P}, \mathbf{\Psi})$ and ADR values were calculated by setting $\mathbf{\Psi}$ to $\mathbf{\Psi}_m$ or $\mathbf{\Psi}_0$ as defined for the results in Fig. 5. To be consistent with the experimental cases, we intentionally set the 2D grids of (μ_s, g) with no grid point coincident with the μ_{sv} and g_v in $\mathbf{P}_V$, which means $\delta_{\min} > 0$ for the virtual samples. The results are plotted in Fig. 6 to compare performance or robustness of $\mathbf{\Psi}_m$ against $\mathbf{\Psi}_0$. It is very interesting to note that the variation of ADR
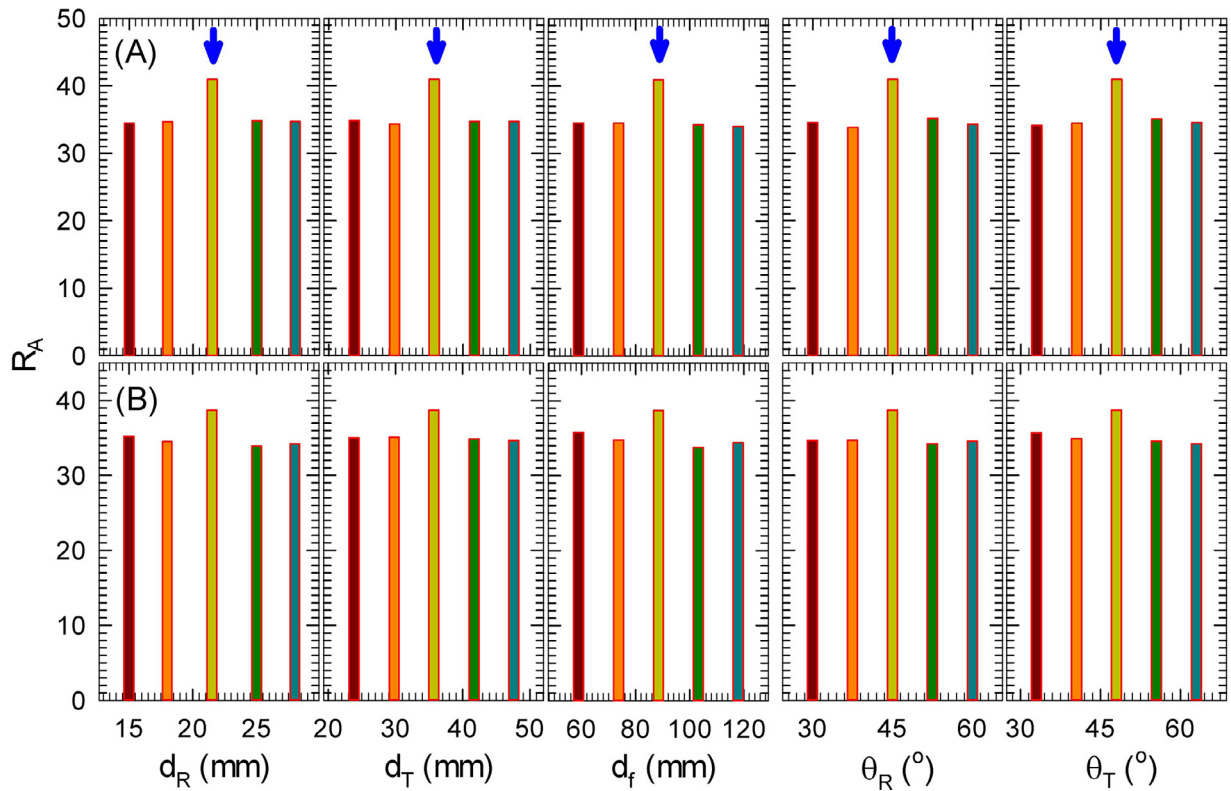
Fig. 5. Comparison of maximum ADR values selected from multiple (μ_s, g) planes for each $\mathbf{\Psi}_m$ or $\mathbf{\Psi}_0$ and the sphere sample represented by $\mathbf{P}_2(\lambda)$: (A) λ = 500 nm, μ_a = 0.248 mm^{-1} for maximum ADR; (B) λ = 800 nm, μ_a = 0.248 mm^{-1} for maximum ADR. The tracked photon number N_0 = 10^8 and total number of iMC simulations of each bar was set to 765. The blue arrows indicate $\mathbf{\Psi}_0$ in both (A) and (B).
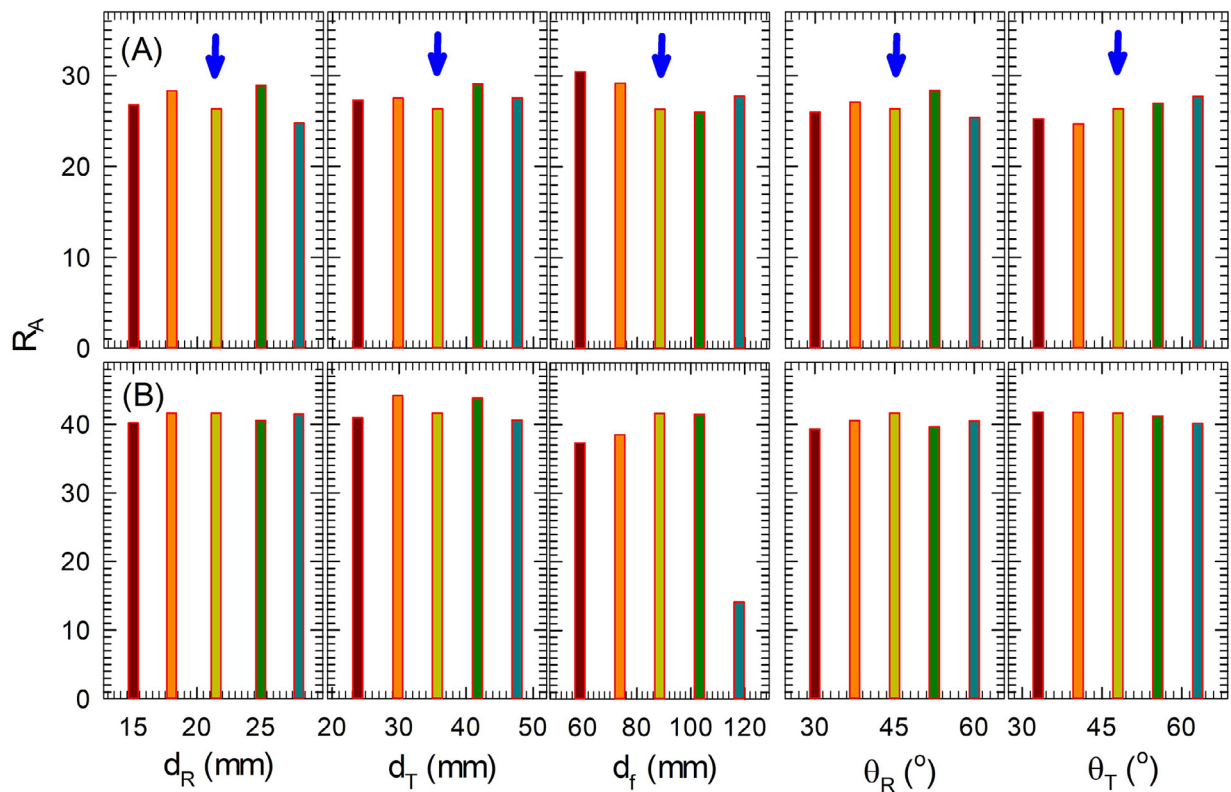

Fig. 6. Comparison of maximum ADR values selected from multiple (μ_s, g) planes of the same μ_{av} among vectors of $\mathbf{\Psi}_m$ and $\mathbf{\Psi}_0$ for a virtual sample represented by $\mathbf{P}_v$: (A) $\mathbf{P}_v$ = (0.597 mm^{-1}, 1.39 mm^{-1},0.907) with a = 0.700; (B) $\mathbf{P}_v$ = (0.288 mm^{-1}, 5.46 mm^{-1}, 0.250) with a = 0.950. The tracked photon number N_0 = 10^8 and total number of iMC simulations of each bar was set to 765. The blue arrows indicate $\mathbf{\Psi}_0$.
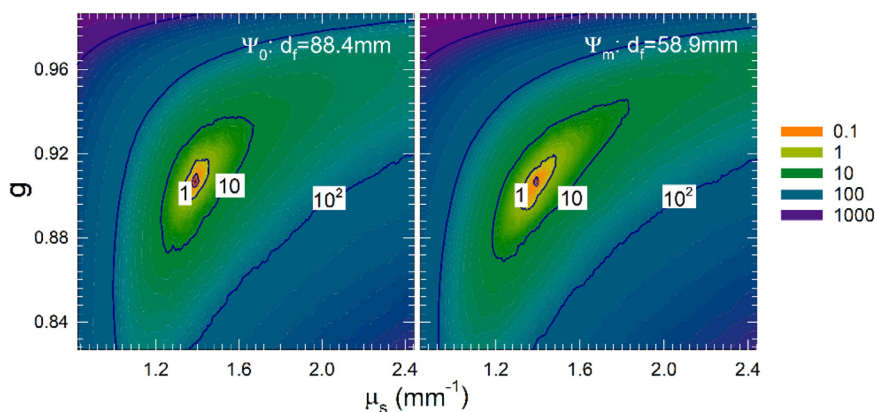
Fig. 7. Contour plots of $\delta(\mathbf{P}, \Psi)$ for the virtual sample of $\mathbf{P}_v = (0.597 \text{ mm}^{-1}, 1.39 \text{ mm}^{-1}, 0.907)$ in Fig. 6(A) with $a = 0.700$ and two detection configurations of Ψ_0 or Ψ_m as noted in each plot. The δ values in percentage are marked on selected contour lines and the legend. The tracked photon number $N_0 = 10^8$ and total number of iMC simulations was 8643 for each plot.

values with either Ψ_0 or Ψ_m is quite small for either sample except the case of $d_f = 118$ mm in Fig. 6(B). Since ADR is determined by global sampling the distribution of δ in a (μ_s, g) plane, similar values of maximal ADR suggest that the robustness of ISP solutions is insensitive to the changes in the configuration of 3-photodiode design. Nevertheless, the very large value of d_f or distance between the sample and detector D_4 leads to very small T_f signal for the virtual sample of nearly isotropic scattering of $g = 0.25$. For this sample, $\delta_{min} = 0.78\%$ and the $A(\delta_1)$ term in Eq. (4) vanishes for all cases of d_f except $d_f = 58.9$ mm and the corresponding ADR values becomes much smaller than that of the case with $d_f = 58.9$ mm.

We compare in Fig. 7 the contour plots in (μ_s, g) planes for the virtual sample of $a = 0.70$ using two different detection configurations of different d_f values. The similarity in the two plots correlate well with the close ADR values shown in Fig. 6(A). Comparing the δ distributions in Figs. 3 and 7, one may further note that strongly turbid samples with large values of a very close to 1, like the case of sphere suspension in this study, present ISPs of increased complexity to solve Eq. (3) due to the existence of long "solution stripes" of $\mu_s(g: \delta < \delta_0)$. For ISPs with smaller values of a as shown in Fig. 7, the stripes shrink markedly and the associated ISP becomes much easier to solve by ADR guided search.

4. Conclusion

This report concerns with the evaluation of ISP solutions for multiparameter spectrophotometry by three non-hemispherically measured signals of scattered light. We have validated an iMC code for accurate modeling of light transport in a turbid sample and signal detection by a 3-photodiode design. The code was applied to obtain distributions of an objective function δ for analysis of ISP types in the 3D space of RT parameter vector $\mathbf{P}$ by selecting a set of contour plots in 2D plane of (μ_s, g). A dimensionless parameter of area descending rate ADR or $R_A(\mathbf{P}, \Psi)$ has been established as an effective metric for evaluating robustness of ISP solutions. ADR values have been determined and compared to quantify the performance and solution robustness of different detection configurations represented by Ψ for various sample types. The results of this study show that the signals of R_d, T_d and T_f measured by the 3-photodiode design allow unique solutions of ISPs in real time and the robustness of solutions is insensitive to variations in Ψ. The presented method of multiparameter spectrophotometry yields an alternative to the integrating sphere based approach with the advantages of system simplicity, ability to measure optically thick samples, fast signal acquisition speed and robustness of ISP solutions.

Declaration of Competing Interest

None.

CRediT authorship contribution statement

Yonghong Qin: Investigation, Software, Data curation. **Peng Tian:** Methodology, Investigation, Software, Data curation. **Lin Zhao:** Software, Investigation. **Stephen M. Mutisya:** Data curation, Writing – review & editing. **Jiahong Jin:** Software, Investigation. **Jun Q. Lu:** Software, Investigation, Writing – review & editing. **Xin-Hua Hu:** Conceptualization, Methodology, Investigation, Software, Data curation, Writing – review & editing.

Acknowledgments

References

[1] Iqbal M, Saeed A, Zafar SI. FTIR spectrophotometry, kinetics and adsorption isotherms modeling, ion exchange, and EDX analysis for understanding the mechanism of Cd2+ and Pb2+ removal by mango peel waste. J Hazard Mater 2009;164:161–71.

[2] Albalasmeh AA, Berhe AA, Ghezzehei TA. A new method for rapid determination of carbohydrate and total carbon concentrations using UV spectrophotometry. Carbohydr Polym 2013;97:253–61.

[3] van de Hulst HC. Multiple Light Scattering: Tables, Formulas and Applications. New York: Academic Press; 1980.

[4] Peters VG, Wyman DR, Patterson MS, Frank GL. Optical properties of normal and diseased human breast tissues in the visible and near infrared. Phys Med Biol 1990;35:1317–34.

[5] Prahl SA, van Gemert MJC, Welch AJ. Determining the optical properties of turbid media by using the adding-doubling method. Appl Opt 1993;32:559–68.

[6] Du Y, Hu XH, Cariveau M, Ma X, Kalmus GW, Lu JQ. Optical properties of porcine skin dermis between 900 nm and 1500 nm. Phys Med Biol 2001;46:167–81.

[7] Ma X, Lu JQ, Ding H, Hu XH. Bulk optical parameters of porcine skin dermis tissues at eight wavelengths from 325 to 1557nm. Opt Lett 2005;30:412–14.

[8] Chen C, Lu JQ, Ding H, Jacobs KM, Du Y, Hu XH. A primary method for determination of optical parameters of turbid samples and application to intralipid between 550 and 1630 nm. Opt Express 2006;14:7420–35.

[9] Friebel M, Roggan A, Muller G, Meinke M. Determination of optical properties of human blood in the spectral range 250 to 1100 nm using Monte Carlo simulations with hematocrit-dependent effective scattering phase functions. J Biomed Opt 2006;11:34021.

[10] Aernouts B, Zamora-Rojas E, Van Beers R, Watte R, Wang L, Tsuta M, et al. Supercontinuum laser based optical characterization of Intralipid phantoms in the 500-2250 nm range. Opt Express 2013;21:32450–67.

[11] Lemaillet P, Cooksey CC, Hwang J, Wabnitz H, Grosenick D, Yang L, et al. Correction of an adding-doubling inversion algorithm for the measurement of the optical parameters of turbid media. Biomed Opt Express 2018;9:55–71.

[12] Xie BW, Ma LX, Zhao JM, Liu LH, Wang XZ, He YR. Experimental study of the radiative properties of hedgehog-like ZnO–Au composite particles. J Quant Spectrosc Radiat Transf 2019;232:93–103.

[13] Bergmann F, Foschum F, Zuber R, Kienle A. Precise determination of the optical properties of turbid media using an optimized integrating sphere and advanced Monte Carlo simulations. Part 2: experiments. Appl Opt 2020;59:3216–26.

[14] Ma CY, Zhao JM, Liu LH, Zhang L, Li XC, Jiang BC. GPU-accelerated inverse identification of radiative properties of particle suspensions in liquid by the Monte Carlo method. J Quant Spectrosc Radiat Transf 2016;172:146–59.

[15] Liang X, Li M, Lu JQ, Huang C, Feng Y, Sa Y, et al. Spectrophotometric determination of turbid optical parameters without using an integrating sphere. Appl Opt 2016;55:2079–85.

[16] Tian P, Mutisya SM, Jin J, Zheng S, Lu JQ, Hu X-H. Spectral determination of μa, μs and g from single and multiple scattering signals with one optically thick sample. J Quant Spectrosc Radiat Transf 2020;245:106868.

[17] Henyey LG, Greenstein JL. Diffuse radiation in the galaxy. Astrophys J 1941;93:70–83.

[18] Tian P, Qin Y, Zhao L, Mutisya SM, Jin J, Lu JQ, et al. Multiparameter spectrophotometry platform for turbid sample measurement by robust solutions of radiative transfer problems. IEEE Trans Instrum Meas 2021;70:6003110.

[19] Chen X, Feng Y, Lu JQ, Liang X, Ding J, Du Y, et al. Fast method for inverse determination of optical parameters from two measured signals. Opt Lett 2013;38:2095–7.

[20] Ma X, Lu JQ, Brock RS, Jacobs KM, Yang P, Hu XH. Determination of complex refractive index of polystyrene microspheres from 370 to 1610 nm. Phys Med Biol 2003;48:4165–72.

[21] Song Z, Dong K, Hu XH, Lu JQ. Monte Carlo simulation of converging laser beams propagating in biological materials. Appl Opt 1999;38:2944–9.

[22] Tian P, Chen C, Jin J, Hong H, Lu JQ, Hu XH. Quantitative characterization of turbidity by radiative transfer based reflectance imaging. Biomed Opt Express 2018;9:2081–94.

[23] Bohren CF, Huffman DR. Absorption and Scattering of Light by Small Particles. New York: Wiley; 1983. p. 477.